Supplemental Document

Biomedical Optics EXPRESS

Three-dimensional virtual histology of the cerebral cortex based on phase-contrast X-ray tomography: supplement

Marina Eckermann,[1,2] Franziska van der Meer,[3] Peter Cloetens,[4] Torben Ruhwedel,[5] Wiebke Möbius,[2,5] Christine Stadelmann,[2,3] and Tim Salditt[1,2,*]

[1] *Institut für Röntgenphysik, Friedrich-Hund-Platz 1, 37077 Göttingen, Germany*
[2] *Cluster of Excellence "Multiscale Bioimaging: from Molecular Machines to Networks of Excitable Cells" (MBExC), University of Göttingen, Germany*
[3] *Institut für Neuropathologie, Robert-Koch-Straße 40, 37075 Göttingen, Germany*
[4] *ESRF, the European Synchrotron, 71, avenue des Martyrs, 38043 Grenoble Cedex 9, France*
[5] *Max-Planck-Institut für experimentelle Medizin, Hermann-Rein-Straße 3, 37075 Göttingen, Germany*
[*] *tsaldit@gwdg.de*

Supplement DOI: https://doi.org/10.6084/m9.figshare.16872859

Parent Article DOI: https://doi.org/10.1364/BOE.434885

3d virtual histology of the Cerebral Cortex based on Phase-Contrast X-ray tomography: supplemental document

SAMPLE PREPARATION

Human hippocampal tissue Human hippocampal tissue was retrieved by surgery or routine autopsy, in agreement with the ethics committee of the University Medical Center Göttingen. Following established clinical pathology protocols, autopsy dissection blocks were fixed in 10% PFA.
For unstained tissue preparations, samples were subsequently dehydrated and paraffin-embedded (FFPE) (if applicable, for non-liquid embedding of samples). A single FFPE-block measured about $2 \times 3 \times 0.3$ cm^3. In all cases, cylindrical samples for PC-CT were extracted using a 1 mm-biopsy punch and inserted into polyimide tubes.
For heavy metal staining, tissue blocks were incubated in 1 % OsO_4 (1-2 h at room temperature, RT), and then infiltrated with propylene oxide in PBS in an increasing series. For embedding, tissue samples were placed in Renlam resin in propylene oxide (1:1, 2:1) prior to incubation in pure resin and polymerization (twice overnight).

Murine brain tissue Male C57Bl6N mice at the age of 10 days were sacrificed in agreement with the ethics committee of Max-Planck-Institute for Experimental Medicine by cervical dislocation. Tissue was fixed by immersion in solution containing 2.5% glutaraldehyde, 4% formaldehyde and 0.5% NaCl in 0.1 M phosphate buffer (PB).
Staining procedure followed either the *conventional-OsO_4* protocol [1], or a modification referred to as *reduced osmium, thiocarbohydrazide, osmium* (rOTO), which further elevates membrane penetration of OsO_4 [2]. The so-called conventional protocol comprised following steps and parameters: Samples were washed in 0.1 M PB (3×10 min at 4°C). After post-fixation and staining in 2% OsO_4 in 0.1 M PB (4 h at 4°C), tissue samples then were washed, dehydrated with increasing concentrations of acetone in water (30%, 50%, 70% and 90%, for 20 mins each at RT), and incubated in 100% acetone (3×15 min). For embedding, tissues were incubated with increasing concentrations of EPON resin mixed with acetone (2:1, 1:1 1:2, for 2 h each at RT) prior to incubation with pure EPON resin (overnight at RT) and polymerization (24 h at 60°C), for which the sample was mounted in a 1 mm-kapton tube.
The rOTO protocol has been conducted as follows: Samples were washed in 0.1 M PB buffer (3×15 mins at 4°C), and then incubated in 2% OsO_4 and 0.25% K4[Fe(CN)6] (3 h at 4°C) to reduce the OsO_4 to OsO_2. After washing with ddH_2O, samples were incubated with 0.1% thiocarbohydrazide (in ddH_2O, for 1 h at RT). Samples were subsequently treated with 2% OsO_4 (90 min), and after washing with ddH_2O, further contrasted with 2.5% uranyl acetate (overnight at 4°C), followed by several washes with ddH_2O. Samples were then dehydrated and resin-embedded, as for the rOTO-preparation.
The sample preparation techniques are illustrated in Fig. 1(d).

EXPERIMENTAL SETUPS - SYNCHROTRON BEAMLINES

The synchrotron-based data presented in this work were collected at two beamlines dedicated to propagation-based holo-tomography: (SR1) the GINIX endstation of the P10 beamline, Petra III, DESY, Hamburg [3], and (SR2) the nano-imaging beamline ID16A, ESRF, Grenoble [4, 5], cf. Fig. S1(a & b).

- **SR1:** GINIX is equipped with two different setups for PC-CT. Overview scans covering FOVs of about 1.5 mm are scanned in *parallel-beam configuration* (PB) [6], depicted in Fig. 1(e). In a continuous rotation, 3000 projections and 200 flat images are recorded with the PCO.edge detector (50 µm Lu:Ag scintillator, $px = 0.65$ µm $10\times$ objective, $M = 1$) in a full 360° rotation. With 35 ms exposure time, a total scan takes about 70 s. Opposing projections

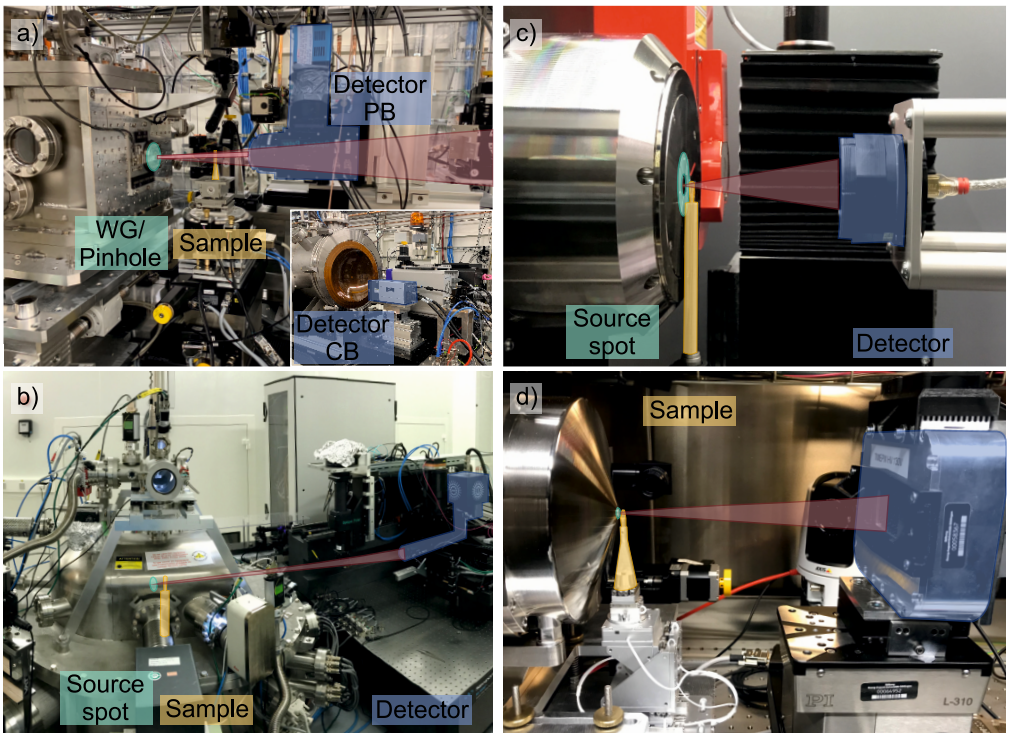

Fig. S1. Annotated photographs of the experimental setups. (Green) marks the X-ray focal plane, (orange) the sample stage, (blue) the detectors. (a) GINIX endstation at P10 beamline, DESY, Hamburg (SR1). In PB-configuration, the PCO.Edge-detector is used ("Detector PB"). The inset shows the detector stage approx. 5 m down stream ("Detector CB" sCMOS-cameras, Photonic Science & Andor). (b) ID16A beamline, ESRF, Grenoble (SR2). (c) EasyTom Nano setup (RX Solutions), with the CCD-camera in use (µCT1). (d) Home-built nanoPC-CT setup TINa, with Excillum NanoTube N2 X-ray source and a single photon counting detector (Timepix) (µCT2).

are used for projection correction in order to mitigate ring-artifacts, and 1500 processed projections serve tomographic reconstruction to fullfill the sampling criteria. In the data shown here, $z_{12} \approx 40$ mm and the further settings detailed in Tab. S1 were used. Fig. 1(f) depicts the *cone-beam geometry* (CB), serving high-resolution data acquisition using a compound optics of KB-mirrors and X-ray waveguides (WG). Data were recorded with a fiber-plate CCD-camera with a 15 µm thick Gadox-scintillator at $z_{02} \approx 5$ m. By changing the distance z_{01} between WG and sample, the geometric magnification M is adjusted: with $M \approx 40...138$, different voxel sizes between $px \simeq 200$ nm and $px \simeq 50$ nm were chosen in this work. Scan-specific details are given in Tab. S2.

	Human, unstained FFPE	Mouse OsO_4 conv.	Mouse rOTO	Human WM OsO_4
Figure	2	7(a.i)	7(b.i)	5(b.iv-v)
E (keV)	13.8	10.8	21.0	10.8
τ (s)	0.035	0.035	0.035	0.035
z_{12} (mm)	41	40	17.5	17.5
px (µm)	0.65	0.65	0.65	0.65
FOV (mm^2) (h×v)	1.7×1.3	1.7×1.3	1.7×1.3	1.7×1.3
d ($\cdot 10^{-3}$ m)	3.0	0.2	3.6	0.2
D ($\cdot 10^4$ Gy)	1.1	2.4	0.2	2.4
F	0.1148	0.0920	0.4089	0.0898
Phase retrieval	NLT	NLT	NLT	NLT
lim1	$8 \cdot 10^{-4}$	$8 \cdot 10^{-4}$	$8 \cdot 10^{-4}$	$8 \cdot 10^{-4}$
lim2	0.05	0.05	0.05	0.05
δ/β	30	15	15	10

Table S1. Scan and reconstruction parameters of GINIX-data recorded in SR1-PB configuration. E denotes the X-ray energy, τ the exposure time, z_{12} the sample-to-detector distance, px the pixel size, FOV the field-of-view in the sample plane, d the attenuation length, D the estimated radiation dose, and F the Fresnel number. lim1/2 are the regularization parameters, and δ/β the ratio of dispersion to absorption decrement of the refractive index.

- **SR2:** ID16A beamline is specialized in nano-holotomography, with voxel sizes down to 10 nm. X-rays are provided either at 17.1 or 33.6 keV photon energy, and focused by KB-mirrors. Here we used 17.1 keV and a propagation distance $z_{12} = 1.2$ m in cone-beam geometry (cf. Fig. 1(f)). Magnified projections were recorded by a lens-coupled FReLoN CCD-camera (23 µm GGG:Eu scintillator). The acquisitions can take advantage of a particularly high flux (approx. $2 \cdot 10^{11}$ ph/s) and a cryo environment under vacuum. The present study was conducted at room temperature under vacuum. Further details are listed in Tab. S2, and the experiment is referenced as [7].

Dose estimation The accumulated dose D in the sample-FOV was estimated as

$$D = \frac{I_0 \tau E}{d \rho_m \mathrm{FOV}},$$

with the usual approximations as discussed in [8, 9], based on photon flux I_0, which was approximated as $I_0 \approx 5 \cdot 10^{11}$ ph/s for SR1-PB, $I_0 \approx 10^9$ ph/s for SR1-CB and $I_0 \approx 2 \cdot 10^{11}$ ph/s for SR2, exposure time τ, X-ray energy E, attenuation length d, mass density ρ_m. For paraffin-embedded samples $\rho_m = 2.2$ g/cm^3 was used, and d as computed by [10] for a representative protein and tissue composite with stochiometry $C_{50}C_{30}N_9O_{10}S_1$ [9]. For stained samples, ρ_m was kept constant, since the dose-damage relationship refers to the energy uptake per tissue mass, rather than label mass. To this end, however. we neglect the additional dose uptake by photoelectrons of larger range, emitted from heavy atom labels into their environment. Instead, the attenuation length d was calculated from the measured X-ray transmission T in the respective projections, based on d_{FFPE} for unstained FFPE-preparations, i.e. $d_{\mathrm{stain}} = \frac{\log(T_{\mathrm{FFPE}})}{\log(T_{\mathrm{stain}})} \cdot d_{\mathrm{FFPE}}$.

	Human, unstained FFPE	Human, unstained Dehyd. Series	Mouse OsO_4 conv.	Mouse rOTO	Human OsO_4	Human OsO_4
Ex. Figure	2	3	7(a.ii-iii)	7(b.ii)	5(b.vi)	5(b.vii-viii)
# projections	1442	1501	1501	1001	1501	1501
# defocus dist.	1	2 (70% Eth.: 3)	4	4	3	2 1/2
E (keV)	8.0	8.0	13.8	13.8	10.8	10.0
τ (s)	2	1	0.7	1	2	0.4
z_{01} (mm)	150	130	125	125	125	40
z_{02} (mm)	5113	5073	5113	5113	5113	5113
px (nm)	200	161	159	159	159	49.2
FOV (mm^2) (h×v)	0.51×0.43	0.33×0.33	0.33×0.33	0.33×0.33	0.41×0.34	0.13×0.11
d ($\cdot 10^{-3}$ m)	0.59	0.45	4.20	1.30	0.19	0.16
D ($\cdot 10^{4}$ Gy)	1.1	1.6	9.4	2.8	34.7	71.3
F	$1.8 \cdot 10^{-3}$	$1.4 \cdot 10^{-3}$	$2.3 \cdot 10^{-3}$	$2.3 \cdot 10^{-3}$	$1.8 \cdot 10^{-3}$	$5.3 \cdot 10^{-4}$
Phase retrieval	NLT	NLT	NLT	NLT	NLT	NLT
lim1	$8 \cdot 10^{-4}$	$8 \cdot 10^{-3}$	$2 \cdot 10^{-2}$	$2 \cdot 10^{-2}$	$5 \cdot 10^{-2}$	$5 \cdot 10^{-2}$
lim2	0.4	0	0.8	0.8	0.05	0.01
δ/β	90	35	30	30	15	25

	Mouse OsO_4 conv.	Mouse rOTO	Mouse rOTO
Ex. Figure	7(a.iv)	7(b.iii)	7(b.iv)
# projections	2000	2000	2000
# defocus dist.	4	4	4
E (keV)	17.1	17.1	17.1
τ (s)	0.2	0.2	0.2
z_{01} (mm)	48.6	48.6	16.4
z_{02} (mm)	1208	1208	1208
px (nm)	130	130	50
FOV (mm^2) (h×v)	0.26×0.26	0.26×0.26	0.10×0.10
d ($\cdot 10^{-3}$ m)	0.75	2.4	2.4
D ($\cdot 10^{6}$ Gy)	7.4	2.4	15.9
F	$2.2 \cdot 10^{-3}$	$2.2 \cdot 10^{-3}$	$8.6 \cdot 10^{-4}$
Phase retrieval	CG	CG	CG
lim1	0	0	0
lim2	0.01	0.01	0.01
δ/β	15	15	15

Table S2. Experimental and reconstruction settings and parameters for (top) SR1-CB and (bottom) SR2 data, recorded in CB-configuration. E denotes the X-ray energy, τ the exposure time, z_{01} the source-to-sample and z_{02} the sample-to-detector distance, px the pixel size, FOV the field-of-view in the sample plane, d the attenuation length, D the estimated radiation dose, and F the Fresnel number. lim1/2 are the regularization parameters, and δ/β the ratio of dispersion to absorption decrement of the refractive index.

EXPERIMENTAL SETUPS - LABORATORY IMPLEMENTATIONS

Laboratory PC-CT (µCT) was conducted with two setups configured for sub-µm imaging: (µCT1) the commercial EasyTom Nano (RX Solutions) [11], and (µCT2) the home-built TINa-setup [12], cf. Fig. S1(c & d).

- **µCT1:** With EasyTom Nano, X-rays were generated by a Hamamatsu transmission-target source (W), and projections were recorded by a CCD-camera (Gadox-scintillator, 9 µm pixels, 2 × 2-binning) with magnification in the range $M \approx 18...52$. Best feature contrast was found at 60 kV acceleration voltage. This setup was used in overview alignment, with px=0.99 µm and middle focal spot mode, or for higher magnification, with px=0.35 µm and small focal spot mode. Further experimental details are given in Tab. S3.
- **µCT2:** With the TINa-setup, the Excillum NanoTube N2 and a Timepix detector (500 µm Si, 55 µm pixels) were used. Also here, the acceleration voltage was set to 60 kV. The source-to-sample distance was particularly small ($z_{01} = 1.4$ mm), resulting in $M \approx 157$ (as required by the larger detector pixel size). Further details are given in Tab. S3.

	µCT1, Overview	µCT1, ROI	µCT2, ROI
# projections	1568	3008	1201
z_{01} (mm)	5	5	1.4
z_{02} (mm)	98	278	218
px (µm)	0.99	0.35	0.35
FOV (mm^2) (h×v)	2.0 × 0.14*	0.7 × 0.47	0.27 × 0.18
τ (s)	12 × 1.7	5 × 10	14 × 9
Source spot mode	middle	small	0.3 µm
Total scan time (h)	9	46	46

Table S3. Experimental and reconstruction parameters for µCT scans. z_{01} denotes the source-to-sample and z_{02} the sample-to-detector distance, px the pixel size, FOV the field-of-view in the sample plane, and τ the exposure time. No pre-filtering of the beams was used. * denotes the FOV of a single tomographic scan; multiple scans have been acquired and combined in this work.

HOLOGRAPHIC & TOMOGRAPHIC RECONSTRUCTION

Projections were first corrected for empty beam and dark images. For synchrotron-based datasets, phase retrieval was carried out using either the linearized *contrast-transfer-function* (CTF) algorithm [13] or a non-linear implementation thereof, both assuming homogeneous object composition. At (SR1), this is implemented via the *non-linear Tikhonov* (NLT) scheme [14], while at (SR2), a conjugate gradient approach is used [15]. These phase retrieval approaches are well-suited for reconstruction of holographic images at small Fresnel numbers $F = \frac{px^2}{z_{\text{eff}}\lambda} \ll 1$, with wavelength λ, and the effective propagation distance $z_{\text{eff}} = z_{12}/M$. Note that these algorithms provide optimal image quality when applied to data sets recorded at four slightly different Fresnel numbers, i.e. at four different defocus distances as indicated in Fig. 1(f) [16]. Phase reconstruction of laboratory data was performed (µCT1) with a simple phase filter (provided by RX-Solutions software), or (µCT2) using the Bronnikov-aided correction (BAC) [17], as also implemented in [14]. Reconstruction parameters are listed in Tab. S1, S2 and S3.
Phase-retrieved projections were used for tomographic reconstruction, performed either by filtered back-projection (FBP, PB-configuration), or a cone-beam (FDK, CB-configuration) algorithm. Note that the GINIX-dataset recorded at $px = 49.2$ nm (cf. Tab S2) was reconstructed with the simultaneous iterations reconstruction technique (SIRT, 400 iterations). All three tomographic reconstruction schemes are implemented in the ASTRA-toolbox [18].

REFERENCES

1. M.-T. Weil, T. Ruhwedel, M. Meschkat, B. Sadowski, and W. Möbius, "Transmission electron microscopy of oligodendrocytes and myelin," in *Oligodendrocytes*, (Springer, 2019), pp. 343–375.

2. Y. Hua, P. Laserstein, and M. Helmstaedter, "Large-volume en-bloc staining for electron microscopy-based connectomics," Nat. Commun. **6**, 7923 (2015).
3. T. Salditt, M. Osterhoff, M. Krenkel, R. N. Wilke, M. Priebe, M. Bartels, S. Kalbfleisch, and M. Sprung, "Compound focusing mirror and x-ray waveguide optics for coherent imaging and nano-diffraction," J. synchrotron radiation **22**, 867–878 (2015).
4. J. C. da Silva, A. Pacureanu, Y. Yang, F. Fus, M. Hubert, L. Bloch, M. Salome, S. Bohic, and P. Cloetens, "High-energy cryo x-ray nano-imaging at the id16a beamline of esrf," in *X-Ray Nanoimaging: Instruments and Methods III*, vol. 10389 (International Society for Optics and Photonics, 2017), p. 103890F.
5. J. C. Da Silva, A. Pacureanu, Y. Yang, S. Bohic, C. Morawe, R. Barrett, and P. Cloetens, "Efficient concentration of high-energy x-rays for diffraction-limited imaging resolution," Optica **4**, 492–495 (2017).
6. J. Frohn, D. Pinkert-Leetsch, J. Missbach-Güntner, M. Reichardt, M. Osterhoff, F. Alves, and T. Salditt, "3d virtual histology of human pancreatic tissue by multiscale phase-contrast x-ray tomography," J. Synchrotron Radiat. **27**, 1707–1719 (2020).
7. P. Cloetens, M. Eckermann, J. Reichmann, T. Salditt, and M. Osterhoff, "3d structure of the human dentate gyrus by holo-tomography: Alzheimer disease vs control," European Synchrotron Radiation Facility (ESRF), doi:10.15151/ESRF-ES-406587724.
8. Q. Shen, I. Bazarov, and P. Thibault, "Diffractive imaging of nonperiodic materials with future coherent x-ray sources," J. synchrotron radiation **11**, 432–438 (2004).
9. M. R. Howells, T. Beetz, H. N. Chapman, C. Cui, J. Holton, C. Jacobsen, J. Kirz, E. Lima, S. Marchesini, H. Miao *et al.*, "An assessment of the resolution limitation due to radiation-damage in x-ray diffraction microscopy," J. Electron Spectrosc. Relat. Phenom. **170**, 4–12 (2009).
10. B. Henke, E. Gullikson, and J. Davis, "X-ray interactions: photoabsorption, scattering, transmission, and reflection at e=50-30000 ev, z=1-92, atomic data and nuclear data tables," Database 2, Center for X-Ray Optics, Lawrence Berkeley National Laboratory (1993).
11. R. X. Solutions, "Easytom nano," (2021).
12. M. Eckermann, M. Töpperwien, A.-L. Robisch, F. van der Meer, C. Stadelmann, and T. Salditt, "Phase-contrast x-ray tomography of neuronal tissue at laboratory sources with submicron resolution," J. Med. Imaging **7**, 013502 (2020).
13. P. Cloetens, W. Ludwig, J. Baruchel, D. Van Dyck, J. Van Landuyt, J. Guigay, and M. Schlenker, "Holotomography: Quantitative phase tomography with micrometer resolution using hard synchrotron radiation x rays," Appl. Phys. Lett. **75**, 2912–2914 (1999).
14. L. M. Lohse, A.-L. Robisch, M. Töpperwien, S. Maretzke, M. Krenkel, J. Hagemann, and T. Salditt, "A phase-retrieval toolbox for x-ray holography and tomography," J. synchrotron radiation **27** (2020).
15. B. Yu, L. Weber, A. Pacureanu, M. Langer, C. Olivier, P. Cloetens, and F. Peyrin, "Evaluation of phase retrieval approaches in magnified x-ray phase nano computerized tomography applied to bone tissue," Opt. Express **26**, 11110–11124 (2018).
16. S. Zabler, P. Cloetens, J.-P. Guigay, J. Baruchel, and M. Schlenker, "Optimization of phase contrast imaging using hard x rays," Rev. Sci. Instruments **76**, 073705 (2005).
17. Y. D. Witte, M. Boone, J. Vlassenbroeck, M. Dierick, and L. V. Hoorebeke, "Bronnikov-aided correction for x-ray computed tomography," J. Opt. Soc. Am. A **26**, 890–894 (2009).
18. W. Van Aarle, W. J. Palenstijn, J. Cant, E. Janssens, F. Bleichrodt, A. Dabravolski, J. De Beenhouwer, K. J. Batenburg, and J. Sijbers, "Fast and flexible x-ray tomography using the astra toolbox," Opt. express **24**, 25129–25147 (2016).